Materials Advances

ROYAL SOCIETY OF CHEMISTRY

PAPER

View Article Online
View Journal | View Issue

Cite this: *Mater. Adv.*, 2025, 6, 3344

Strategic design of binary transition metal sulfides for superior asymmetric supercapacitors†

Junaid Khan, *[ab] A. Ahmed [c] and Abdullah A. Al-Kahtani[d]

Received 19th January 2025,
Accepted 21st April 2025

DOI: 10.1039/d5ma00052a

rsc.li/materials-advances

Transition metal sulfides have emerged as promising materials for asymmetric supercapacitors due to their excellent electrochemical properties, including high specific capacitance and superior cycling stability. These characteristics offer significant potential for advancing energy storage technologies with improved performance and efficiency. In this study, a series of bimetallic sulfides were synthesized by systematically varying the nickel-to-cobalt ratio, starting from individual phases of NiS_2 and CoS_2. Among the prepared compositions, $Ni_{0.5}Co_{0.5}S_2$ demonstrated the most outstanding electrochemical behavior, achieving a high specific capacity of 1710 C g^{-1} at a scan rate of 0.002 V s^{-1}. When employed as the anode material in an asymmetric supercapacitor device, it delivered an impressive energy density of 120 W h kg^{-1} at a power density of 1020 W kg^{-1}. Notably, even at a high power density of 8510 W kg^{-1}, the device retained a substantial energy density of 36 W h kg^{-1}. Furthermore, the device exhibited excellent long-term cycling performance, maintaining 96% of its initial capacity after 4000 continuous charge–discharge cycles at a current density of 10 A g^{-1}. These findings highlight the strong potential of $Ni_{0.5}Co_{0.5}S_2$ as an efficient and durable electrode material for next-generation high-performance asymmetric supercapacitor systems.

1. Introduction

As the depletion of fossil fuel reserves accelerates and the urgency to mitigate global warming intensifies, researchers worldwide are striving to harness renewable and sustainable energy sources such as wind, tidal power, and solar energy. Alongside these efforts, significant attention is being directed toward the development of high-performance and cost-effective energy storage devices (ESDs) to complement and stabilize these renewable energy systems. Among the various ESDs, supercapacitors have garnered substantial research interest due to their remarkable attributes, including excellent cyclic stability and superior specific power (P).[1–3] Despite these advantages, supercapacitors face a critical limitation: their specific energy (E) is considerably lower than that of batteries, which hampers their commercial viability.[4] In response to this challenge, growing attention has been directed toward asymmetric supercapacitors (AS), which offer a strategic blend of two distinct electrode types: one mimicking battery behavior by utilizing redox-based (faradaic) charge storage for enhanced energy capacity, and the other functioning like a conventional capacitor, depending on surface-driven (non-faradaic) processes to ensure rapid power output.[5] By leveraging the distinct electrochemical properties of both electrode types, ASs can enhance the E_s of the system while extending the operating voltage range through the utilization of different potential windows suitable for each electrode. Consequently, the selection of optimal materials for the positive (anode) and negative (cathode) electrodes, both compatible with the same electrolyte, is critical to achieving high-performance AS. The performance of AS is predominantly influenced by the morphology and properties of the material used in electrodes.[6,7] The materials with battery-grade nature exhibit higher faradaic activity and storage capability, making them attractive candidates for energy storage applications.[8,9] Activated carbon (AC) remains the material of choice in negative electrode due to its affordability, facile synthesis, high surface area, and excellent electrical properties.[10,11] In contrast, transition metal hydroxides and oxides have been extensively investigated for use as battery-type electrode materials owing to their outstanding pseudocapacitive properties.[12–16] These materials offer significantly higher specific capacitance compared to carbonaceous materials. In addition to metal oxides, transition metal phosphates such as $Ni(PO_4)_2$, $Co(PO_4)_2$, and $NiCo(PO_4)_2$ have emerged as promising candidates for electrode materials in ESDs due to their excellent electrochemical potential.[17] However, these materials are not without challenges.[18,19] Their practical application in AS is often limited by issues such as structural instability, which can

[a] *Department of Physics, Government Postgraduate Collage No. 1, Abbottabad, Khyber Pakhtunkhwa, Pakistan. E-mail: junaidkhan.nanotech@gmail.com*
[b] *Department of Higher Education Achieves and Libraries, Government of Khyber Pakhtunkhwa, Pakistan*
[c] *Department of Chemical and Bilogical Engineering, Gachon University, 1342 Seongnam-daero, Seongnam 13120, Republic of Korea*
[d] *Chemistry Department, Collage of Science, King Saud University, P. O. Box 2455, Riyadh-11451, Saudi Arabia*

† Electronic supplementary information (ESI) available. See DOI: https://doi.org/10.1039/d5ma00052a

lead to capacity fading, as well as low electrical conductivity and slow ion diffusion, which restrict rate capability.[20,21] Addressing these challenges remains a critical focus for advancing the performance of asymmetric supercapacitors.

Transition metal sulfides have garnered significant attention in recent years due to their exceptional electrical conductivity, diverse oxidation states, and remarkable electrochemical performance.[22] Compounds such as CoS_2, NiS, NiS_2, and Ni_3S_4 have been successfully synthesized and demonstrate outstanding potential as electrode materials in supercapacitor devices.[23,24] Notably, the synthesis of two-dimensional (2D) tin sulfide nanostructures, a groundbreaking study revealed that these 2D tin sulfide-based supercapacitors exhibit high mechanical flexibility, areal capacitance, and stability in structure.[25] Among transition metal sulfides, cobalt and nickel sulfides are recognized for their remarkable electronic properties and energy storage applications.[26,27] However, its exploration as an electrode material for supercapacitors (SCs) remains underdeveloped. Compared to oxides and phosphates, research on transition metal sulfides is still in its nascent stages. Multiple recent literature underscore the potential of transition metal sulfides as advanced materials for energy storage applications. Ref. 28 emphasize that incorporating a secondary metal into the configuration of oxides and sulfides enhances their catalytic activity and cycling efficiency. Various bimetallic sulfides, including flower-shaped Zn–Co sulfides, hollow Cu–Co sulfide spheres, and Co–Mo–S nanosheets, have been extensively explored with superior electrochemical performance. These developments provide significant insights into the design and synthesis of bimetallic transition metal sulfides as efficient electrode materials. However, challenges such as low rate capability, limited energy density, and poor cycling stability continue to impede their broader application in portable energy storage systems. Despite substantial progress in the development of bimetallic sulfides for energy storage, the strategic tuning of metal compositions to optimize structural stability and electrochemical behavior remains underexplored. Various synthesis strategies have been developed to fabricate metal sulfide nanomaterials with tailored properties suitable for energy storage applications. These methods include sol–gel processing, co-precipitation, solvothermal treatment, sonochemical techniques, chemical vapor deposition, microwave-assisted synthesis, and hydrothermal methods.[29] Each approach offers distinct advantages in terms of morphology control, crystallinity, and process scalability. Among them, the hydrothermal method has emerged as a particularly attractive route due to its operational simplicity, cost-effectiveness, and ability to yield highly crystalline products.[30] This technique involves conducting chemical reactions in a sealed vessel at elevated temperatures and pressures, enabling precise control over phase formation and particle size. Furthermore, hydrothermal synthesis is well-suited for producing nanostructures with uniform morphology without requiring high-temperature post-treatment. These features make it especially effective for developing nanomaterials with optimized electrochemical characteristics for use in supercapacitors and other energy storage devices.

This work aims to bridge that gap by systematically investigating cobalt–nickel sulfide ($Ni_xCo_{(1-x)}S_2$) compositions synthesized *via* a simple hydrothermal method, enabling precise control over morphology and phase formation. The novelty of this study lies in the comparative analysis of multiple Ni/Co ratios and their influence on electrochemical properties, ultimately identifying an optimal composition for high-performance asymmetric supercapacitor devices. The outcomes provide a promising pathway toward low-cost, high-efficiency electrode materials tailored for next-generation hybrid energy storage applications.

2. Materials and methods

All materials were obtained from Sigma-Aldrich. To fabricate cobalt sulfide (CoS_2), a solution was prepared by dissolving 0.1 moles of cobalt nitrate hexahydrate ($Co(NO_3)_2{\cdot}6H_2O$) in 25 mL of deionized water, referred to hereafter as solution A. For mixed-metal sulfide precursors, a separate mixture was created by combining 0.025 moles of nickel nitrate hexahydrate ($Ni(NO_3)_2{\cdot}6H_2O$) and 0.075 moles of cobalt nitrate hexahydrate in 20 mL of deionized water—this was characterized solution B. To synthesize an equimolar (50 : 50) composition of nickel and cobalt sulfide ($Ni_{0.5}Co_{0.5}S_2$), another precursor was made by dissolving 0.05 moles each of $Ni(NO_3)_2{\cdot}6H_2O$ and $Co(NO_3)_2{\cdot}6H_2O$ in 20 mL of DI water, designated as solution C. Similarly, solution D was prepared for producing $Ni_{0.75}Co_{0.25}S_2$ by mixing 0.075 moles of $Ni(NO_3)_2{\cdot}6H_2O$ and 0.025 moles of $Co(NO_3)_2{\cdot}6H_2O$ in the same volume of DI water. For pure nickel sulfide (NiS_2), 0.1 moles of $Ni(NO_3)_2{\cdot}6H_2O$ were dissolved in 20 mL of DI water to form solution E. Following a 10-minute pre-stirring phase, 0.374 grams of sodium sulfide were added to solution A, which was then stirred for an additional 40 minutes. The resulting mixture was transferred into a stainless steel autoclave lined with Teflon and subjected to hydrothermal treatment at 180 °C for 24 hours. After cooling, the resulting black precipitate was isolated *via* centrifugation washed and finally dried in a vacuum oven at 75 °C for 8 hours. The obtained cobalt sulfide product was labeled as sample S1. An identical synthesis route was followed for solutions B, C, D, and E to obtain $Ni_{0.25}Co_{0.75}S_2$, $Ni_{0.5}Co_{0.5}S_2$, $Ni_{0.75}Co_{0.25}S_2$, and NiS_2, which were designated as samples S2, S3, S4, and S5, respectively. A schematic overview of the entire synthesis process is illustrated in Fig. 1.

Electrode slurries for samples were formulated by blending 80% of the active material (4.00 mg) with 10% acetylene black (AB) and 10% polyvinylidene fluoride as a binder, using *N*-methyl-2-pyrrolidone as the dispersing agent. The mixture was stirred continuously for 8 hours to ensure homogeneity. Once thoroughly mixed, the slurry was uniformly applied onto precleaned nickel foam substrates (2 mm thick) measuring 1 × 1 cm^2, which served simultaneously as the support and current collector. Following the coating process, the electrodes were dried at 70 °C for 9 hours to remove any residual solvent and ensure proper adhesion of the active layer. Subsequently, electrochemical evaluations were carried out using a GAMRY reference 3000 Potentiostat/Galvanostat system. All measurements

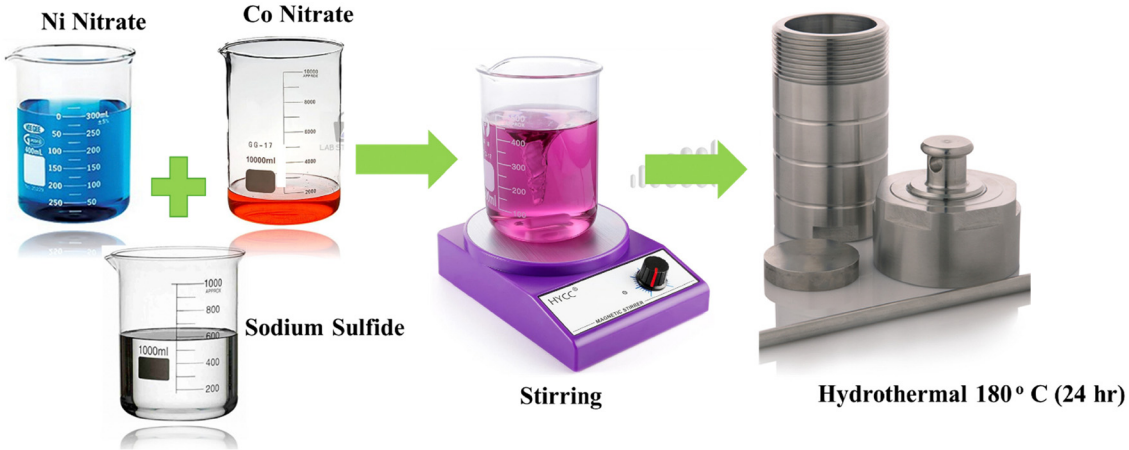

Fig. 1 Synthesis route of bi-metallic sulfide.

were performed in an aqueous electrolyte composed of 1 M potassium hydroxide.

3. Results and discussion

3.1. Structural and surface characterization

The X-ray diffraction (XRD) analysis, which is an essential technique for determining crystalline structures and phase purity is carried out. The XRD patterns of all prepared sulfides are illustrated in Fig. S1 (ESI†). For sample S1, the diffraction peaks at 18.0, 19.9, 22.3, 24.6, 25.9, 30.1, 33.6, 38.2, 42.1, and 52.8 degree corresponds to planes (111), (200), (210), (211), (220), (311), (222), (321), (400), and (511), exhibit a precise match with the standard reference pattern in JCPDS card No. 10-0408. The sharpness and intensity of the peaks further indicate the high crystallinity of the synthesized CoS_2 phase. Similarly, the XRD spectrum of sample S5 reveals distinct diffraction peaks at 31.2, 34.1, 38.2, 43.1, 55.0, 59.6, and 74.1 degree representing (100), (002), (101), (102), (110), (103), (112) planes that closely correspond to JCPDS card No. 01-088-1711, signifying the formation of an orthorhombic nickel sulfide (NiS_2) structure. The prominent peaks in this pattern attest to the successful synthesis and phase purity of the nickel sulfide material. In contrast, the XRD patterns of intermediate samples S2, S3, and S4 display characteristic peaks that align with both JCPDS card No. 10-0408 (cobalt sulfide) and JCPDS card No. 01-088-1711 (nickel sulfide). This dual correspondence clearly indicates the formation of nickel-cobalt binary sulfides, wherein the co-existence of cobalt and nickel sulfide phases demonstrates the successful incorporation of both metal elements into the crystal lattice. The broad and overlapping peaks observed in these samples may suggest a synergistic interaction between cobalt and nickel sulfides, leading to the formation of a mixed-phase or partially alloyed structure. These results highlight the structural adaptability and compositional diversity achieved through precise control of the hydrothermal synthesis parameters, paving the way for the design of advanced materials with tunable properties for energy storage applications.

The synthesized sulfide nanomaterials were analyzed using energy-dispersive X-ray spectroscopy (EDX) to determine their elemental makeup. Fig. S2–S6 (ESI†) present the EDX results for samples S1 through S5. In the spectra for S2, S3, and S4, peaks confirm the presence of sulfur, cobalt, and nickel. Specifically, sample S1 exhibits distinct peaks for cobalt and sulfur, while sample S5 displays clear indicators for nickel and sulfur. The absence of any extraneous peaks in the spectra further confirms the high purity of the synthesized nanomaterials.

Fig. 2 presents the SEM images of the synthesized sulfide samples captured at a magnification of 500 nm, providing a detailed view of their morphologies. The SEM analysis reveals distinct morphological features across the samples, which play a critical role in determining their charge storage behavior. The S1 exhibits a flake-like morphology characterized by thin, overlapping layers. This structure significantly increases the surface area, facilitating enhanced material and electrolyte interaction. However, the diminutive size of these flakes poses a limitation, as it slightly hinders ion mobility and charge transfer, thereby marginally reducing the sample's electrochemical activity. In contrast, the S5 sample, consisting of nickel sulfide, displays an irregular, highly porous morphology resembling cotton-like structures. This porous architecture improves the accessibility of electrolytes, promotes efficient ion diffusion, and facilitates enhanced charge transfer. The SEM images of the intermediate samples (S2, S3, and S4), where nickel sulfide is incorporated into cobalt sulfide, reveal a progressive enhancement in porosity compared to the S1 sample. This structural evolution introduces well-defined voids and interconnected channels, which significantly improve the penetration and diffusion of electrolyte ions. The synergy between the increased porosity of nickel sulfide and the flaky morphology of cobalt sulfide contributes to enhanced redox activity and superior electrochemical performance. In summary, the incorporation of nickel sulfide into cobalt sulfide not only refines the structural features of the material but also amplifies its charge storage capacity and ionic conductivity. These improvements render the composite material highly promising for application in energy storage devices. The nitrogen adsorption–desorption

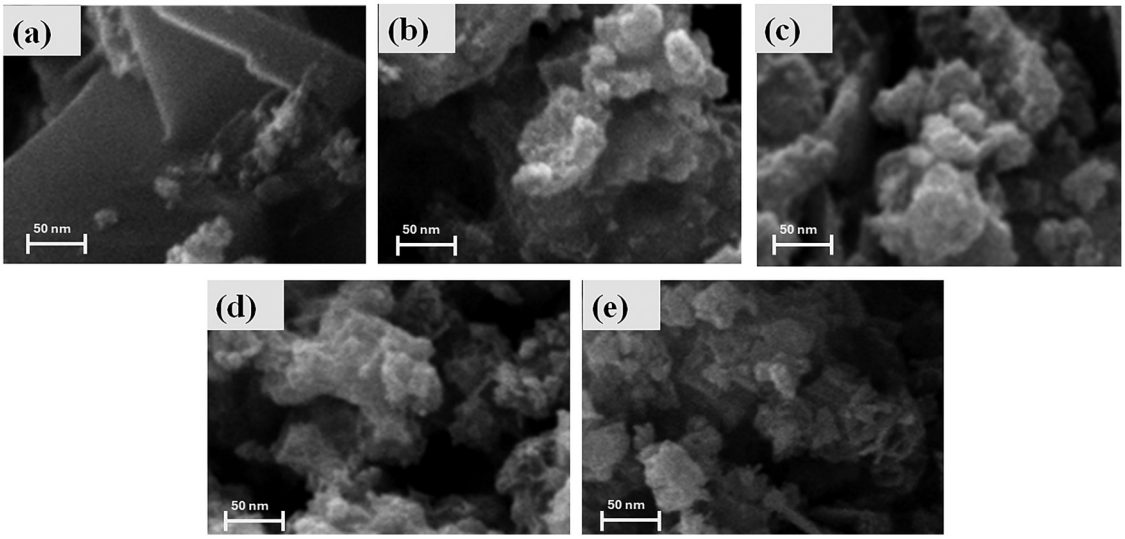

Fig. 2 (a–e) SEM images of S1, S2, S3, S4, and S5 correspondingly at similar magnification.

isotherms of all the synthesized samples have been presented in Fig. S7 (ESI†). The specific surface area was found to be 151.9, 154.8, 421.6, 332.2, and 198.6 $m^2\ g^{-1}$ for samples S1 to S5, respectively. The results brace the SEM claim.

3.2. Electrochemical characterization

Cyclic voltammetry (CV) was performed to evaluate the electrochemical properties of the synthesized materials. The CV measurements were conducted for all the electrodes using a three-electrode configuration at multiple scan rates with the potential window fixed at 0 to 0.7 V. The CV profiles of all the samples are comparatively presented in Fig. 3(a) at 10 mV s^{-1}. All the samples display distinct anodic and cathodic current peaks, reflecting the presence of reversible redox interactions between hydroxide ions (OH^-) and the electrode surfaces—behavior typically associated with battery-type materials.[31] Notably, the incorporation of nickel sulfide into cobalt sulfide (S2, S3, and S4) resulted in an enhanced peak current, indicating improved performance.

The specific capacity Q_s (C g^{-1}) was calculated as:[32,33]

$$Q_s = \frac{1}{mv}\int_{vi}^{vf} I \times V \mathrm{d}V \quad (1)$$

here, the integral part corresponds to the area under CV curve. From Figure, it is obvious that S3 holds the dominant state with the higher area under the CV curve. The CV profile of S3 at multiple scan rates is presented in Fig. 3(b) The analysis revealed that higher potential sweep rates correspond to increased peak currents, further emphasizing the materials' capability for rapid charge–discharge cycles. The determined charge storage capability through CV results for all the samples is depicted in Fig. 3(c). The Q_s values for S1, S2, S3, S4 and S5 are 560, 1230, 1710, 790 and 1260 C g^{-1}, respectively. The log(voltage) and log(peak current) relationship for all synthesized sulfide samples, as demonstrated in Fig. 3(d), reveals *b*-values of 0.46, 0.55, 0.51, 0.47, and 0.58 for S1, S2, S3, S4, and S5, respectively. These values confirm that the synthesized nanomaterials exhibit predominantly battery-like behavior.

The galvanostatic charge–discharge (GCD) was employed to evaluate the electrochemical performance S1–S5 samples. At a fixed potential window (0–0.6 V), various current densities were used. The discharge profile of all the samples recorded at current density of 3.0 A g^{-1} is comparatively presented in Fig. 4(a). The nonlinear characteristics observed in all sulfide samples suggest the occurrence of faradaic reactions. The specific charge (Q_s) and specific capacitance (C_s) were calculated from the GCD curves using the following equations:[33,34]

$$Q_s = \Delta t \times \frac{I}{m} \quad (2)$$

$$C_s = \frac{I \times \Delta t}{m \times \Delta V} \quad (3)$$

In the relevant equations, the variables "m", "I", "ΔV", and "Δt" represent the mass of the active electrode material, applied current, voltage window, and discharge duration, respectively. Eqn 2 and 3 clearly demonstrate that materials with longer discharge durations under constant current conditions possess higher charge storage capacities. Fig. 4(a) highlights that sample S3 exhibits the longest discharge period, indicating superior storage behavior. The GCD curves of dominant S3 are presented in Fig. 4(b), recorded is multiple current densities. The symmetrical nature of the GCD plateaus reflects the reversibility of the redox processes, highlighting the excellent rate capability of the prepared electrode.

All the electrodes are tested at multiple current densities and Fig. 5(a) and (b) display the observed Q_s and C_s for all the samples at corresponding current densities. The highest recorded values for Q_s (C_s) for S1 through S5 are as follows: S1 – 340 C g^{-1} (560 F g^{-1}), S2 – 440 C g^{-1} (740 F g^{-1}), S3 – 800 C g^{-1}

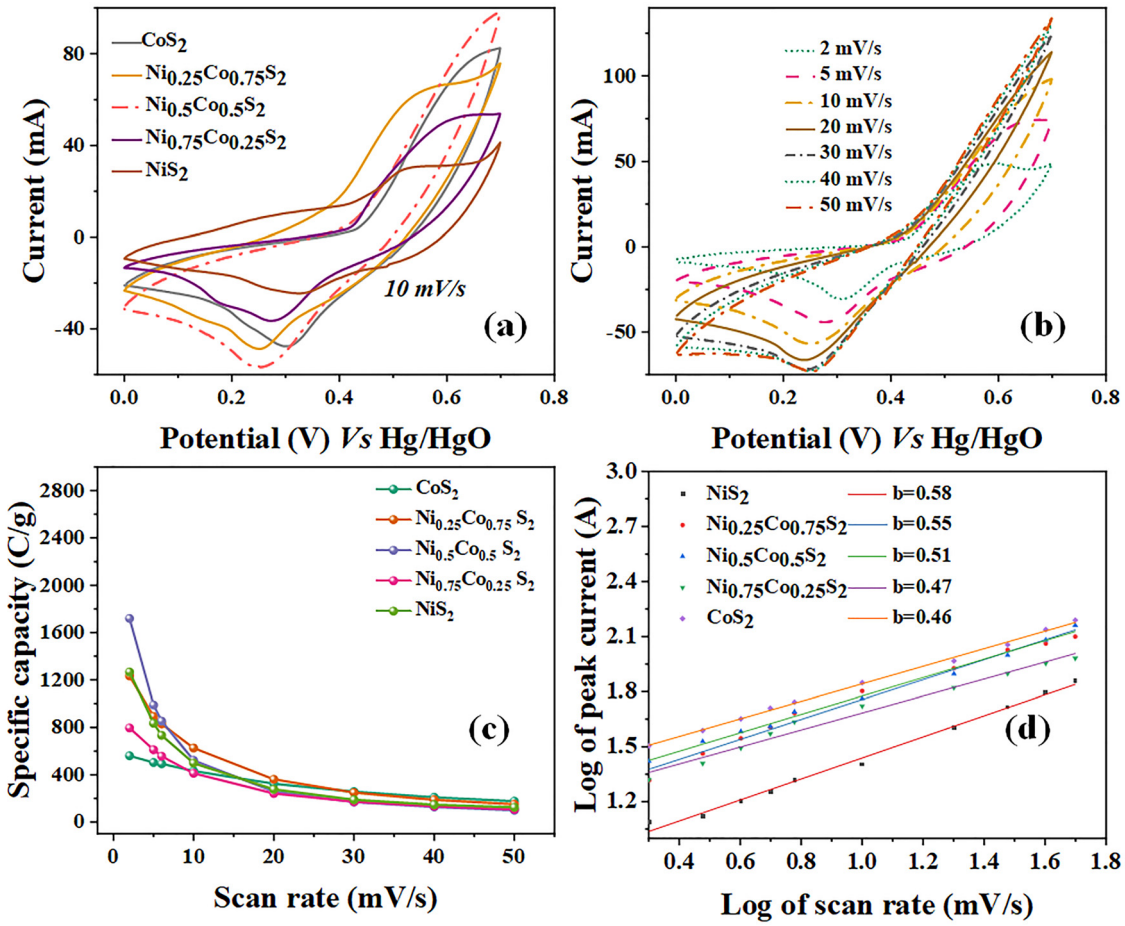

Fig. 3 (a) CV profiles of all the samples recorded at the scan rate of 10 mV s^{-1}, elucidating their redox active nature, (b) CV profile of S3 with dominant performance among all, (c) Q_s calculated for all the samples while being tested at different sweep rates, and (d) *b*-value fitting for all the samples.

(1340 F g^{-1}), S4 – 380 C g^{-1} (640 F g^{-1}), and S5 – 540 C g^{-1} (900 F g^{-1}). It was also observed that storage capability declined at higher current densities. This reduction is attributed to limited time for electrolyte ion transport and reduced interaction of electrode material with ionic species. Overall, S3 emerged as the most efficient electrode in terms of electrochemical behavior, as evidenced by the GCD analysis.

Electrochemical impedance spectroscopy (EIS) was performed, providing insights into their electrochemical behavior and performance under practical conditions. The analysis was

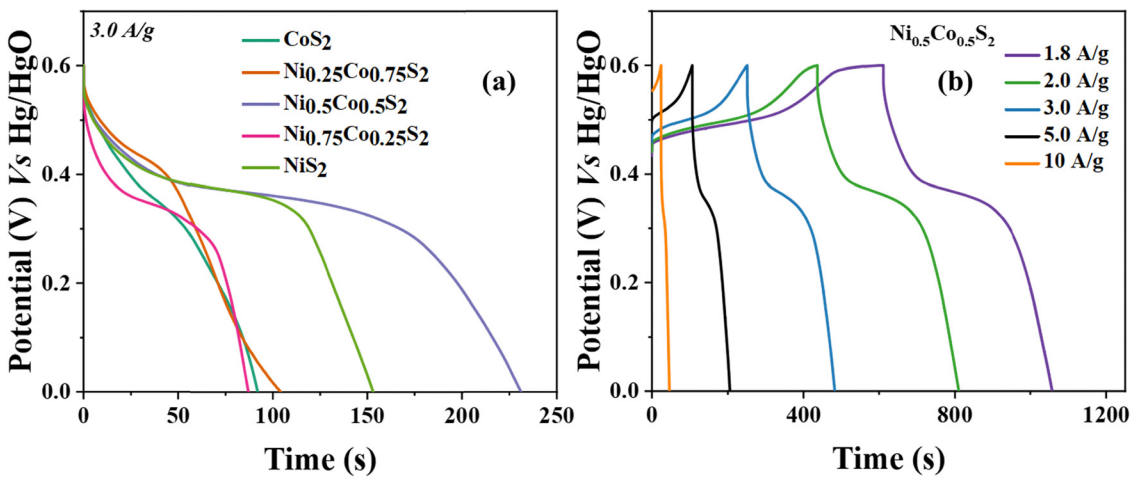

Fig. 4 (a) Discharge curves of all the samples at current density of 3 A g^{-1}. (b) GCD results of S3 at different current density values.

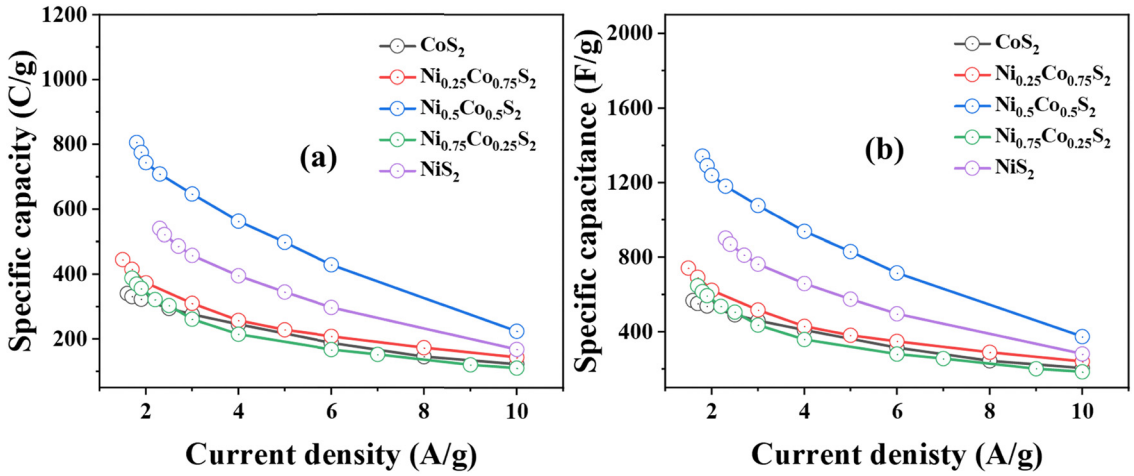

Fig. 5 Calculated (a) Q_s and (b) C_s trend against multiple current densities.

conducted using a three-electrode configuration across a broad frequency range of 0.1 Hz to 100 000 Hz, allowing for a comprehensive examination of both high-frequency and low-frequency processes. Fig. 6(a) presents the Nyquist plots for all synthesized sulfide samples. In the high-frequency region, the *x*-intercept of the Nyquist plot was utilized to estimate the equivalent series resistance (E_s), which is a crucial parameter that signifies the resistance at the interface of electrolyte and electrode. To evaluate the charge transfer characteristics, an equivalent circuit model was utilized, as illustrated in the inset. This model comprises the load resistance (Rl), charge transfer resistance (R_{ct}), equivalent series resistance (R_s), and two constant phase elements (C1 and C2), which account for the non-ideal capacitive behavior at the electrode–electrolyte interface. The obtained values are presented in Table 1. For sample S1, the E_s value was 2.1 Ω, indicating a relatively high interfacial resistance at this stage. Interestingly, upon introducing 25% nickel sulfide into the composition (sample S2), the E_s value decreased to 1.3 Ω, reflecting improved electrolyte-ion interaction and charge transfer. A further increase in nickel sulfide content (sample S3 with 50% nickel sulfide) resulted in the lowest E_s value of 0.9 Ω, signifying optimal interface conductivity. However, with a composition of 75% nickel sulfide in sample S4, the E_s slightly increased to 1.0 Ω, and in S5 (100% nickel sulfide), the ESR reached the highest value of 1.4 Ω. This indicates that the nickel sulfide composition plays a pivotal role in governing the charge transfer kinetics and interfacial resistance. The decrease in the semicircle diameter in the high-frequency region for S3 suggests its superior charge transfer resistance (R_{ct}) when compared to other samples. Lower R_{ct} values correspond to enhanced conductivity and faster electron transfer kinetics, indicating better performance under electrochemical conditions. Additionally, S3 exhibited a near-vertical line in the low-frequency region as opposed to S2, which suggests a significantly reduced Warburg resistance (Wd). This phenomenon implies that S3 promotes faster ion transport and improved diffusion kinetics, key parameters for efficient energy storage devices.[35,36] The low-frequency response of the Nyquist plot offers valuable information regarding ionic transport pathways within the electrode material. It was observed that the structural design of S3 provides a more extended and efficient ion diffusion pathway. This extended pathway facilitates the rapid movement of electrolyte ions toward the active sites of the electrode, thereby improving ionic conductivity and electrochemical performance. Furthermore, the analysis indicated that the unique structural properties of S3, influenced by its 50% nickel sulfide composition, are well-suited for energy storage applications as they balance the competing effects of ionic mobility and charge transfer

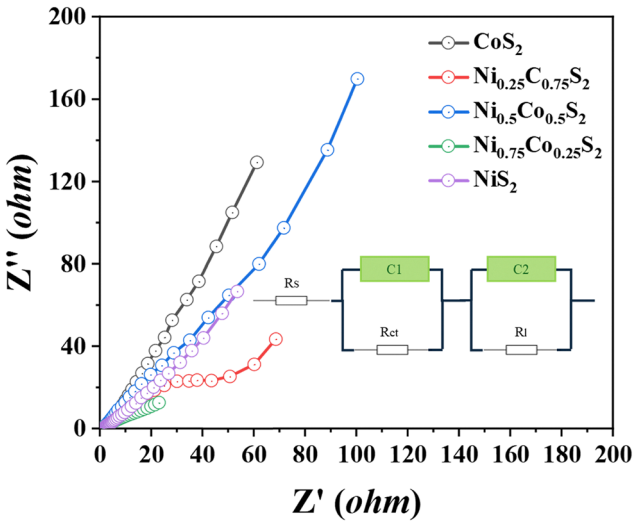

Fig. 6 EIS outcomes of all the samples in Nyquist plot.

Table 1 Simulated EIS outcomes

Sample	E_s Ω	R_{ct} Ω
S1	2.1	1.9
S2	1.3	1.4
S3	0.9	0.8
S4	1.0	1.1
S5	1.4	1.3

resistance. This improved performance is likely a result of optimized porosity and structural homogeneity, allowing better accessibility for electrolyte ions and faster reaction kinetics. The findings from the EIS analysis align well with the results obtained from galvanostatic charge–discharge (GCD) and cyclic voltammetry (CV) studies. These complementary electrochemical techniques confirmed that sample S3 consistently demonstrated superior performance in terms of specific capacitance, rate capability, and cycling stability within the three-electrode setup. Collectively, the comprehensive EIS, GCD, and CV data strongly support the deduction that S3 displays the most favorable electrochemical behavior among all the synthesized nanomaterials, highlighting its potential as an efficient electrode material for advanced energy storage applications.

3.3. Asymmetric supercapacitors (AS)

An AS device was designed to explore the practical potential of the optimized configuration of bimetallic sulfide. In this configuration, activated carbon was employed as the negative electrode, while S3—demonstrating superior performance in the three-electrode setup—served as the active material for the positive (anode) electrode. A thin, highly permeable separator was introduced between these two electrodes to facilitate the efficient movement of electrolyte ions. In operation, the AC electrode functions over a potential window (PW) from 0 to −1 V, while S3 operates within a range from 0 to 0.7 V. The cyclic voltammetry (CV) curves of both electrodes at a scan rate of 3 mV s^{-1} are depicted in Fig. 7(a), illustrating the distinct diffusive and capacitive mechanisms of interaction between the two electrodes. Furthermore, these results highlight the functional operational potential window of the hybrid device (0–1.7 V). Fig. 7(b) displays the CV profiles recorded over varying sweep rates, providing insights into the electrochemical behavior across these rates. Notably, the symmetrical nature of the CV profiles at elevated scan rates further underscores the excellent stability and rate capability of the fabricated AS device, confirming its promising performance characteristics.

The galvanostatic charge–discharge (GCD) analysis of the AS device was carried out within an operational potential window (PW) of 0 to 1.7 V, while systematically varying the current densities. The GCD is illustrated in Fig. 8(a), demonstrating reversible storage mechanisms. The Q_s of the ASs was extracted different current densities, as shown in Fig. 8(b). The device exhibited a maximum Q_s value of 512 C g^{-1} at a current density of 1.2 A g^{-1}. To assess the cyclic stability, the S3//AC device underwent 4000 continuous GCD cycles at a current density of 10 A g^{-1}. The corresponding capacity retention data is presented in Fig. 8(c), revealing that the device maintains 96% of its initial charge storage capability after 4000 cycles, indicating excellent stability over prolonged operation. Electrochemical impedance spectroscopy (EIS) was employed to examine the conductivity of the S3//AC device across a frequency range of 0.1 to 100 000 Hz. The Nyquist plot for this analysis is shown in Fig. 9(a). The figure confirms that the S3//AC device has an initial equivalent series resistance (ESR) of 0.34 Ω. Furthermore, the charge-transfer resistance is found to be 4.28 Ω. The E(W h kg^{-1}) and P(W kg^{-1}) of AS were calculated as:[33]

$$E_s = \frac{Q_s}{2} \times \frac{\Delta V}{3.6} \quad (4)$$

$$P_s = \frac{E_s}{\Delta t} \times 3600 \quad (5)$$

Fig. 9(b) illustrates the power densities (P) of the ASs device as a function of their corresponding energy densities (E). The developed AS device achieves a remarkable energy density of 120.9 W h kg^{-1} paired with a power density of 1020 W kg^{-1} at a current density of 1.2 A g^{-1}. Even at a higher current density of 10 A g^{-1}, it retains a substantial energy density of 36.3 W h kg^{-1} and delivers an outstanding power density of 8512 W kg^{-1}. These performance metrics clearly surpass those of many recently reported nanomaterial-based systems.[37–50]

4. Conclusion

In conclusion, nickel and cobalt sulfides with systematically varying ratios were successfully synthesized through a simple and

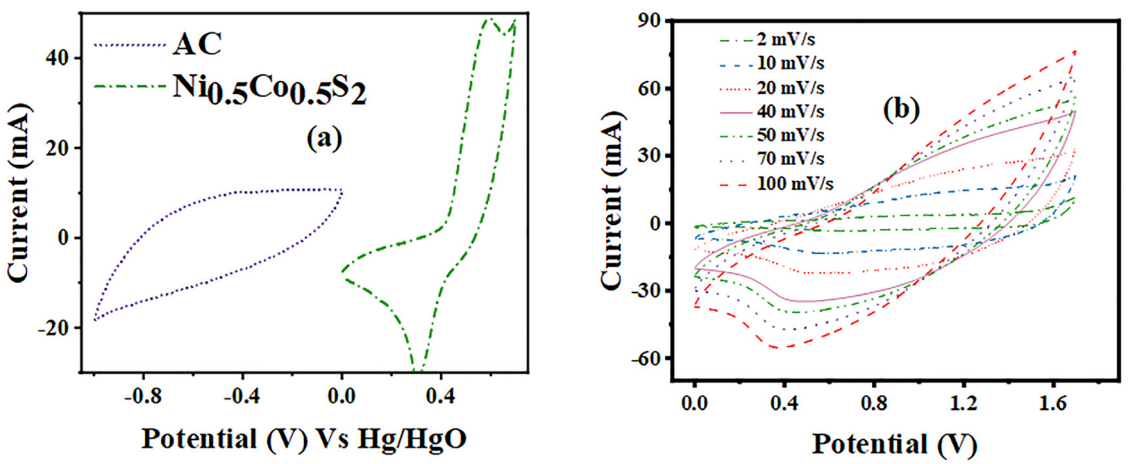

Fig. 7 CV profile of (a) S3 and AC in three cell configurating elaborating their different storage mechanisms, (b) S3//AC real device.

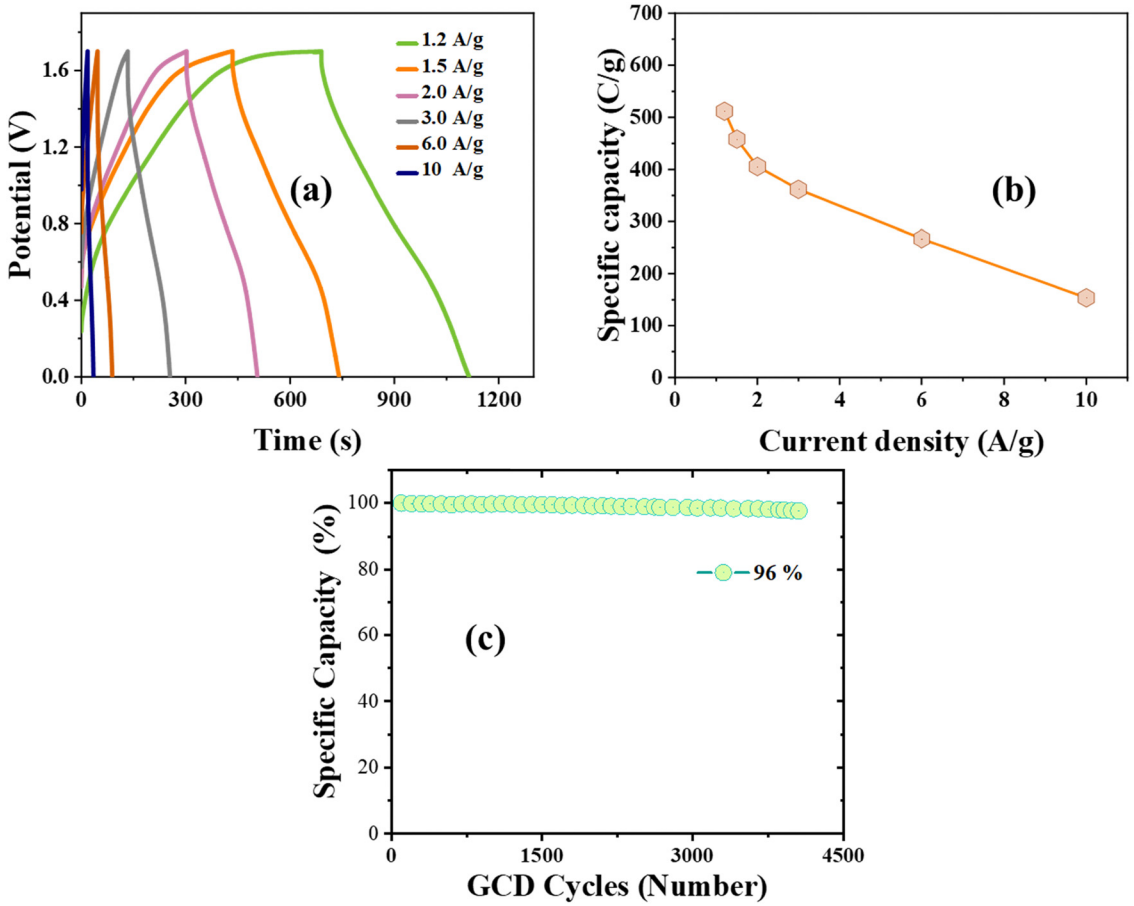

Fig. 8 (a) S3//AC real device GCD, (b) Q_s and (c) stability test result.

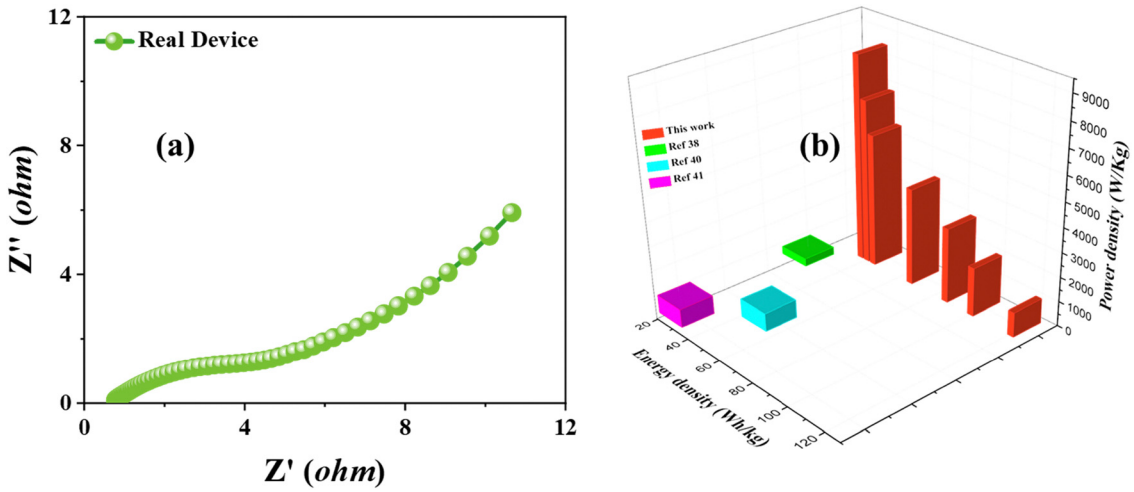

Fig. 9 (a) real device EIS (b) *E* and *P* obtained from real device.

efficient hydrothermal method. The structural, morphological, and elemental characteristics of the synthesized sulfides were meticulously characterized using energy-dispersive X-ray spectroscopy (EDX), scanning electron microscopy (SEM), and X-ray diffraction (XRD) analyses. Electrochemical performance was evaluated employing a three-electrode configuration, with $Ni_{0.5}Co_{0.5}S_2$ exhibiting the most promising performance with a specific capacity of 1710 C g^{-1} at a scan rate of 2 mV s^{-1} and 800 C g^{-1} (1340 F g^{-1}) at a current density of 1.8 A g^{-1}. Furthermore, the S3// AC device demonstrated an impressive specific capacity of 512 C g^{-1}, a notable *E* of 120 W h kg^{-1}, and *P* of 1020 W kg^{-1} at a current density of 1.2 A g^{-1}. Furthermore, at a higher current

density of 10 A g^{-1}, the device maintained a E of 36 W h kg^{-1} and achieved an outstanding P of 8510 W kg^{-1}, highlighting its superior rate capability. Notably, after 4000 cycles at 10 A g^{-1}, the device retained 96% of its initial capacity, demonstrating excellent cycling stability. These remarkable electrochemical properties underscore the great promise of $Ni_{0.5}Co_{0.5}S_2$ as an effective and reliable positive electrode material for advanced asymmetric supercapacitor technologies.

Data availability

The data will be made available on request.

Conflicts of interest

There are no conflicts to declare.

Acknowledgements

The authors thank the ''researchers supporting project number (RSP2025R266), King Saud university, Riyadh, Saudi Arabia'' for their financial support.

References

1 X. Zhang, C. Jiang, J. Liang and W. Wu, Electrode materials and device architecture strategies for flexible supercapacitors in wearable energy storage, *J. Mater. Chem. A*, 2021, **9**(13), 8099–8128.
2 S. M. Benoy, M. Pandey, D. Bhattacharjya and B. K. Saikia, Recent trends in supercapacitor-battery hybrid energy storage devices based on carbon materials, *J. Energy Storage*, 2022, **52**, 104938.
3 X. Chen, P. Chang, S. Zhang, L. Guan, G. Ren and J. Tao, Nano-dendrite structured cobalt phosphide based hybrid supercapacitor with high energy storage and cycling stability, *Nanotechnology*, 2021, **33**(8), 085403.
4 F. Xing, Z. Bi, F. Su, F. Liu and Z. S. Wu, Unraveling the Design Principles of Battery-Supercapacitor Hybrid Devices: From Fundamental Mechanisms to Microstructure Engineering and Challenging Perspectives, *Adv. Energy Mater.*, 2022, **12**(26), 2200594.
5 S. Ahmed, M. Gondal, A. Alzahrani and M. Almessiere, Critical review on transition metal selenides/graphene composite as futuristic electrode material for high performance supercapacitors, *J. Energy Storage*, 2023, **74**, 109214.
6 D. Lee, N. Shinde, J. C. Ding, J. Fu, R. K. Sahoo and H. W. Lee, *et al.*, Improvement of electrical performance by surface structure of Ni-material as a high-performance asymmetric supercapacitor electrode, *Ceram. Int.*, 2020, **46**(8), 11189–11197.
7 Y. Gao, B. Wu, J. Hei, D. Gao, X. Xu and Z. Wei, *et al.*, Self-assembled synthesis of waxberry-like open hollow $NiCo_2S_4$ with enhanced capacitance for high-performance hybrid asymmetric supercapacitors, *Electrochim. Acta*, 2020, **347**, 136314.
8 Y. Tang, W. Guo and R. Zou, Nickel-based bimetallic battery-type materials for asymmetric supercapacitors, *Coord. Chem. Rev.*, 2022, **451**, 214242.
9 Z. Xu, C. Du, H. Yang, J. Huang, X. Zhang and J. Chen, NiCoP@ CoS tree-like core-shell nanoarrays on nickel foam as battery-type electrodes for supercapacitors, *Chem. Eng. J.*, 2021, **421**, 127871.
10 P. Sinha, S. Banerjee and K. K. Kar, Activated carbon as electrode materials for supercapacitors, *Handbook of Nanocomposite Supercapacitor Materials II: Performance*, 2020, pp. 113–144.
11 J. Khan, Enhanced supercapacitor performance using EG@COF: a layered porous composite, *RSC Adv.*, 2025, **15**, 11441.
12 K. Y. Kumar, S. Archana, R. Namitha, B. Prasanna, S. Sharma and M. Raghu, Ruthenium oxide nanostring clusters anchored Graphene oxide nanocomposites for high-performance supercapacitors application, *Mater. Res. Bull.*, 2018, **107**, 347–354.
13 Y. Fan, Z. Ma, L. Wang, Y. Dong, T. Jiang and Z. Li, *et al.*, In-situ synthesis of NiO foamed sheets on Ni foam as efficient cathode of battery-type supercapacitor, *Electrochim. Acta*, 2018, **269**, 62–69.
14 N. Shakeel and J. Khan, Morphology-driven electrochemical attributes of Cu-MOF: a high-performance anodic material for battery supercapacitor hybrids, *RSC Adv.*, 2024, **14**, 33941.
15 R. Teimuri-Mofrad, E. Payami, A. Piriniya and R. Hadi, Green synthesis of ferrocenyl-modified MnO2/carbon-based nanocomposite as an outstanding supercapacitor electrode material, *Appl. Organomet. Chem.*, 2022, **36**(5), e6620.
16 A.-L. Brisse, P. Stevens, G. Toussaint, O. Crosnier and T. Brousse, Ni (OH) 2 and NiO based composites: battery type electrode materials for hybrid supercapacitor devices, *Materials*, 2018, **11**(7), 1178.
17 A. G. Temam, A. Alshoaibi, S. A. Getaneh, C. Awada, A. C. Nwanya and P. M. Ejikeme, *et al.*, Recent progress on phosphate-based electroactive materials for supercapacitor applications, *Surf. Interfaces*, 2023, **13**, 100154.
18 C. Wang, Y. Liu, Y. Sun, L. Cui and J. Liu, 3D nanoflower-like and core–shell structured MCo 2 O 4@ MCo 2 S 4@ polypyrrole (M= Cu, Mn) composites as supercapacitor electrode materials with ultrahigh specific capacitances, *J. Mater. Chem. A*, 2023, **11**(14), 7639–7651.
19 Q. Chen, Z. Wu, L. Zhu, C. Li, X. Zhu and Y. Sun, High mass loading porous CoNi 2 S 4 nanosheets with ultrahigh areal capacity for flexible supercapacitors, *J. Mater. Chem. A*, 2024, **12**(3), 1816–1825.
20 A. A. Kulkarni, N. K. Gaikwad, A. P. Salunkhe, R. M. Dahotre and T. S. Bhat, Transition metal phosphates: a paradigm for electrochemical supercapacitors, *J. Electroanal. Chem.*, 2023, 117795.
21 K. Yuan, T.-J. Gao, Y. Yang, W. Luo, S. Li and C.-Y. Zhang, *et al.*, Template sacrificial controlled synthesis of

hierarchical nanoporous carbon@ NiCo2S4 microspheres for high-performance hybrid supercapacitors, *Rare Met.*, 2023, **42**(8), 2643–2657.

22 H. Rafique, M. W. Iqbal, S. M. Wabaidur, H. ul Hassan, A. M. Afzal and T. Abbas, *et al.*, The supercapattery designed with a binary composite of niobium silver sulfide ($NbAg_2S$) and activated carbon for enhanced electrochemical performance, *RSC Adv.*, 2023, **13**(19), 12634–12645.

23 L. Zheng, Z. Xiao, X. Wang, Y. Xi, S. Zhai and X. Fu, *et al.*, Biomass-Assisted Construction of Carbon-Supported Fe–Co–Cu Trimetallic Oxides/Sulfides for Supercapacitors with Excellent Performance. ACS Applied Energy, *Materials*, 2023, **6**(21), 10862–10873.

24 M. A. Irham, F. H. T. Baskoro, A. Al Ghiffari, D. R. Rodiansyah, A. Wibowo and F. Muttaqien, *et al.*, Unveiling the role of dopants in boosting CuS supercapacitor performance: insights from first-principles calculations, *Phys. Chem. Chem. Phys.*, 2024, **26**(37), 24577–24584.

25 J. Khan, From design to efficiency: cobalt-based MOFs for efficient and stable electrocatalysis in hydrogen and oxygen evolution reactions, *RSC Adv.*, 2025, **15**, 8420–8429.

26 J. Li, *Design of Anionic Redox Materials for High− performance Aluminum−ion Battery*, University of Macau, 2023.

27 N. Sarkar, S. R. Mishra, V. Gadore, B. Panigrahi and M. Ahmaruzzaman, Nanocosmos of catalysis: a voyage through synthesis, properties, and enhanced photocatalytic degradation in nickel sulfide nanocomposites, *Nanoscale Adv.*, 2024, **6**(11), 2741–2765.

28 A. M. Afzal, M. Awais, A. Yasmeen, M. W. Iqbal, S. Mumtaz and M. Ouladsmane, *et al.*, Exploring the redox characteristics of porous ZnCoS@ rGO grown on nickel foam as a high-performance electrode for energy storage applications, *RSC Adv.*, 2023, **13**(31), 21236–21248.

29 J. Ali, S. Guo, Y. Chen, A. Shahzad, M. W. Ullah and F. Chen, Metal sulfides as emerging materials for advanced oxidation of wastewater: Recent developments, challenges, and prospects, *Coord. Chem. Rev.*, 2024, **509**, 215765.

30 S. Alam, Q. Z. Khan, A. Gassoumi, M. I. Khan, M. Z. Iqbal and Z. Ahmad, Innovating synthesis approaches in advancing electrochemical efficiency: A journey into hydrothermal and sonochemical realms, *J. Energy Storage*, 2024, **78**, 109821.

31 J. Khan, M. Z. Iqbal, B. Rubab, F. Jamshaid, A. Khan and N. Shakeel, *et al.*, Isonicotinic acid-based copper-MOF: An exotic redox propertied electrode material for high energy asymmetric supercapacitor, *J. Energy Storage*, 2023, **72**, 108655.

32 S. Vijayakumar, S. Nagamuthu and G. Muralidharan, Supercapacitor studies on NiO nanoflakes synthesized through a microwave route, *ACS Appl. Mater. Interfaces*, 2013, **5**(6), 2188–2196.

33 M. Z. Iqbal, A. Ahmed, J. Khan, S. Alam, A. A. lfseisi and S. Aftab, *et al.*, Exploring the electrochemical potential of redox-active mixed metal sulfide as an efficient electrode material for supercapacitor-battery hybrid, *J. Mater. Sci.*, 2023, **58**(35), 14109–14120.

34 M. Z. Iqbal and J. Khan, Optimization of cobalt-manganese binary sulfide for high performance supercapattery devices, *Electrochim. Acta*, 2021, **368**, 137529.

35 Z. Bo, Z. Huang, Z. Zheng, Y. Chen, J. Yan and K. Cen, *et al.*, Accelerated ion transport and charging dynamics in more ionophobic sub-nanometer channels. Energy Storage, *Materials*, 2023, **59**, 102797.

36 H. Zhang, Y. Geng, J. Huang, Z. Wang, K. Du and H. Li, Charge and mass transport mechanisms in two-dimensional covalent organic frameworks (2D COFs) for electrochemical energy storage devices, *Energy Environ. Sci.*, 2023, **16**(3), 889–951.

37 A. M. Zardkhoshoui, B. Ameri and S. S. H. Davarani, A high-energy-density supercapacitor with multi-shelled nickel–manganese selenide hollow spheres as cathode and double-shell nickel–iron selenide hollow spheres as anode electrodes, *Nanoscale*, 2021, **13**(5), 2931–2945.

38 Y. A. Dakka, J. Balamurugan, R. Balaji, N. H. Kim and J. H. Lee, Advanced $Cu_{0.5}Co_{0.5}Se_2$ nanosheets and MXene electrodes for high-performance asymmetric supercapacitors, *Chem. Eng. J.*, 2020, **385**, 123455.

39 Q. Lu, T. Zhou, B. Zi, J. Zhao, D. Li and M. Chen, *et al.*, Dual supports by cation vacancies and surface optimization for CoNiSe2-based hybrid supercapacitors with high energy density, *ACS Energy Lett.*, 2023, **8**(8), 3420–3429.

40 L. Cheng, S. Chen, Q. Zhang, Y. Li, J. Chen and Y. Lou, Hierarchical sea-urchin-like bimetallic zinc–cobalt selenide for enhanced battery-supercapacitor hybrid device, *J. Energy Storage*, 2020, **31**, 101663.

41 X. Li, W. Sun, L. Wang, Y. Qi, T. Guo and X. Zhao, *et al.*, Three-dimensional hierarchical self-supported $NiCo_2O_4$/carbon nanotube core–shell networks as high performance supercapacitor electrodes, *RSC Adv.*, 2015, **5**(11), 7976–7985.

42 F. Zhang, T. Zhang, X. Yang, L. Zhang, K. Leng and Y. Huang, *et al.*, A high-performance supercapacitor-battery hybrid energy storage device based on graphene-enhanced electrode materials with ultrahigh energy density, *Energy Environ. Sci.*, 2013, **6**(5), 1623–1632.

43 Z. Ling, Z. Wang, M. Zhang, C. Yu, G. Wang and Y. Dong, *et al.*, Sustainable synthesis and assembly of biomass-derived B/N co-doped carbon nanosheets with ultrahigh aspect ratio for high-performance supercapacitors, *Adv. Funct. Mater.*, 2016, **26**(1), 111–119.

44 C. Wang, D. Wu, H. Wang, Z. Gao, F. Xu and K. Jiang, A green and scalable route to yield porous carbon sheets from biomass for supercapacitors with high capacity, *J. Mater. Chem. A*, 2018, **6**(3), 1244–1254.

45 R. Ding, L. Qi, M. Jia and H. Wang, Facile and large-scale chemical synthesis of highly porous secondary submicron/micron-sized $NiCo_2O_4$ materials for high-performance aqueous hybrid AC-$NiCo_2O_4$ electrochemical capacitors, *Electrochim. Acta*, 2013, **107**, 494–502.

46 S. Ahmed, M. Parvaz, R. Johari and M. Rafat, Studies on activated carbon derived from neem (azadirachta indica) bio-waste, and its application as supercapacitor electrode, *Mater. Res. Express*, 2018, **5**(4), 045601.

47 J. He, Y. Zhou, S. Wu, J. Cao, B. Han and Z. Wang, *et al.*, Unlocking the Capacity and Stability Limitations of Perovskite Electrodes and Achieving the Design of a Flame-Retardant Supercapacitor Through the ''Tree Canopy'' Structure, *ACS Energy Lett.*, 2025, **10**, 1680–1687.
48 P. Aghamohammadi, F. Karakaya Mert, E. T. Akgul, N. Aghabalapoor Keshtiban, O. C. Altıncı and A. Gelir, *et al.*, Synthesis, Characterization, and Theoretical Modeling of 2D Molybdenum Boride (MBene) for All Solid-State Flexible Interdigitated Supercapacitor Application, *ACS Omega*, 2025, **10**(8), 8202–8212.
49 J. Wu, Y. Chen, X. Liang, M. Demir and W. Bian, Synergistic effects of MXene and Co_3O_4 in composite electrodes: High-performance energy storage solutions, *J. Electroanal. Chem.*, 2024, **975**, 118720.
50 Y. Qiao, G. Liu, R. Xu, R. Hu, L. Liu and G. Jiang, *et al.*, $SrFe_{1-x}Zr_xO_{3-\delta}$ perovskite oxides as negative electrodes for supercapacitors, *Electrochim. Acta*, 2023, **437**, 141527.